



1     **Effect of double diffusion processes in the deep ocean on the**  
2             **distribution and dynamics of particulate and dissolved**  
3             **matter: a case study in Tyrrhenian Sea**

4  
5     Xavier DURRIEU DE MADRON<sup>1\*</sup>, Paul BLIN<sup>1</sup>, Mireille PUJO-PAY<sup>2</sup>, Vincent  
6     TAILLANDIER<sup>3</sup>, Pascal CONAN<sup>2,4</sup>

7     <sup>(1)</sup> CEFREM, CNRS-Université de Perpignan Via Domitia, Perpignan, France

8     <sup>(2)</sup> LOMIC, CNRS-Sorbonne Université, Banyuls/Mer, France

9     <sup>(3)</sup> LOV, CNRS-Sorbonne Université, Villefranche/Mer, France

10    <sup>(4)</sup> OSU STAMAR, CNRS-Sorbonne Université, Paris, France

11    *Correspondence to:* Xavir Durrieu de Madron (demadron@univ-perp.fr)

12

13    **Abstract:** This study examines CTD, ADCP and optical data collected during the PERLE-3  
14    cruise in March 2020 between the surface and 2000 m depth over an east-west section of the  
15    Tyrrhenian Sea in the Mediterranean. The focus will be on the impact of double diffusion  
16    processes, in particular salt fingering, on the distribution and dynamics of particulate and  
17    dissolved matter. The staircases develop at the interface between the warm, salty Levantine  
18    Intermediate Water (LIW) and the colder, less salty Tyrrhenian Deep Water (TDW) in the  
19    centre of the basin with low hydrodynamic energy. The results show that thermohaline  
20    staircases formed by salt fingering significantly influence particle sedimentation and  
21    biogeochemical cycling in deep ocean environments by altering vertical flux patterns. These  
22    density steps create distinct vertical layers that act as physical barriers, slowing the descent of  
23    particles and facilitating their retention and aggregation. Retention of fine particles at density  
24    gradients promotes the formation of larger aggregates, affecting particle size distribution. The  
25    staircases also affect dissolved matter by creating pronounced concentration gradients of  
26    oxygen and nutrients, which can influence microbial activity and nutrient cycling.

27

28    **Keywords:** Mediterranean, Tyrrhenian Sea, Double diffusion, Salt fingering, Suspended  
29    particulate matter, Particle size spectra, Nitrate, Mineralization

30



31 **1. Introduction**

32 Gravitational settling of biologically derived particles, produced by marine plankton in  
33 the surface layer, is the primary driver of vertical fluxes of material in the deep ocean (Newton  
34 and Liss, 1990). In general, vertical mass fluxes of particles in the ocean decrease exponentially  
35 with depth due to particle degradation and the increasing density of seawater (Omand et al.,  
36 2020). Marine particles have a wide range of sizes, from micrometres (clays) to centimetres  
37 (organic detritus). Particles generally tend to agglomerate to form aggregates of different sizes,  
38 shapes, densities, and characteristics (Kiko et al., 2022). The change in geometry of the  
39 aggregates as well as their excess density compared to seawater are the factors that determine  
40 their sedimentation rate.

41 The water column in the ocean is composed by the superposition of water masses with  
42 distinct thermohaline characteristics and often distant origins. Large density interfaces,  
43 associated with strong vertical gradients in temperature ( $\sim 0.25$  °C/m) at seasonal thermoclines,  
44 or salinity ( $\sim 0.5$  g/kg/m) at river plumes can occur in the upper ocean, resulting in the retention  
45 of the less dense particles. In the deep ocean temperature and salinity gradients are much  
46 weaker, and the effect of particle size becomes greater than the effect of density excess, so that  
47 settling velocity generally increases with particle size. Thus settling velocities in the open ocean  
48 is on the order of  $5 \times 10^{-4}$  mm/s to 1 mm/s for particles ranging from 2  $\mu\text{m}$  to 300  $\mu\text{m}$  (McCave,  
49 1975).

50 However, in the deep ocean, in the transition zones between two water masses, areas of  
51 enhanced density gradients can occur due to double diffusion processes, in particular those  
52 associated with salt fingers. Salt fingering is a common process in the ocean (Radko, 2013). It  
53 requires a stably stratified water column, where a layer of warm, salty water overlies a layer of  
54 cooler, less salty water. Because molecular diffusion of temperature is about 100 times faster  
55 than that of salinity, the salinity interface initially remains essentially unchanged as temperature  
56 exchange occurs across it. As a result, the saltier water above this thin mixed layer of average  
57 temperature becomes denser than the less salty water below. Such thermohaline diffusive  
58 convection leads to salt finger instabilities at the interface: the saltier water sinks and the less  
59 salty water rises. The mixing process is then repeated at the new interfaces, resulting in a  
60 progressive thickening of the mixed layer and an increase in the vertical density gradients on  
61 either side of the interface. If favourable conditions persist, step structures can develop and  
62 reach thicknesses of several tens of meters. These staircases exhibit typical temperature and  
63 salinity gradients on the order of 0.01 °C/m and 0.005 g/kg/m, respectively.

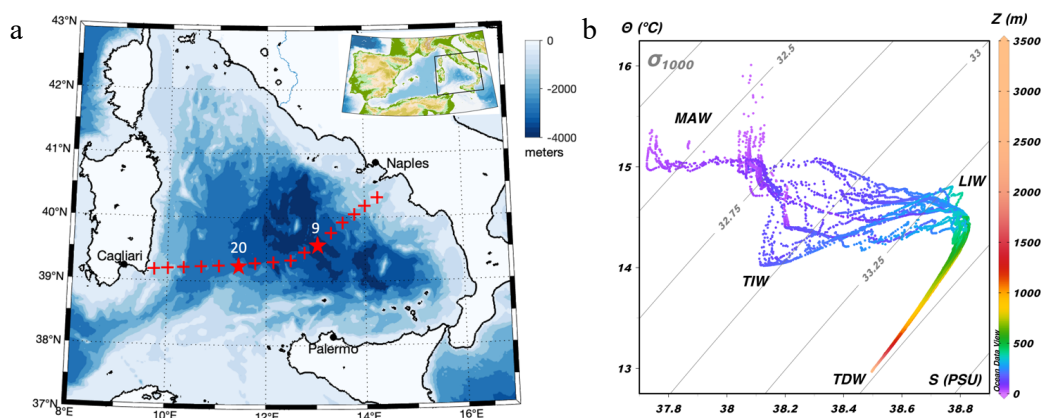
64 There is also the case of a layer of turbid water overlying clearer, denser water, such as  
65 for hypopycnal particle-laden river plumes (e.g. Green, 1987; Hoyal et al., 1999; Hoshiba et al.,  
66 2021). Instabilities may arise as a result of the different diffusivities of each of the constituents  
67 (sediment, temperature, salinity) (Parsons and Garcia, 2000). Both double diffusive and settling  
68 driven convection processes can drive fingering and mixing at the interface, and therefore,  
69 double diffusive sedimentation can add up to the gravitational settling velocity and enhance the  
70 scavenging of particles from the buoyant turbid plume. However, for large particles and dilute  
71 concentrations, the flux is more dominated by gravitational settling and the double diffusive  
72 sedimentation of suspended particles is considered negligible (e.g. Davarpanah Jazi and Wells,  
73 2016).



74 Various experimental and numerical studies have explored the impact of density  
75 interfaces on the sedimentation of particulate material, but to our knowledge very little research  
76 has been applied to the deep oceanic environment. Laboratory experiments conducted for a  
77 variety of individual particles geometries and densities (e.g. Prairie et al., 2013; Mrokowska,  
78 2018; Doostmohammadi and Ardekani, 2014; Doostmohammadi and Ardekani, 2015; Verso et  
79 al., 2019) generally show a decrease in settling velocity, as well as a reorientation of the  
80 particles, during its passage through the transition layer formed by the density interface. The  
81 initial decrease is followed by an increase, once the particle reaches the base of the interface,  
82 but this settling velocity is always smaller in the lower layer due to its higher density. The initial  
83 decrease in velocity in the interface is likely due to the entrainment of less dense water by the  
84 particles and the drag of their wake as they cross the interface. Finally, Maggi (2013) shows  
85 that sedimentation rates are very well correlated with size for mineral particles, but are much  
86 less clear for biomineral or biological material. Thus, the sedimentation rate of a solid particle  
87 alone will depend almost exclusively on its size. This is not the case for aggregates, where  
88 composition, shape, excess density and porosity must also be taken into account. Kindler et al.  
89 (2010) demonstrated that slowly sinking particles, like highly porous aggregates, can be  
90 retained and therefore accumulate at density interfaces, increasing the likelihood of collisions  
91 and subsequent aggregation. They suggested that this increase in retention time may affect  
92 carbon transformation through increased microbial colonization and utilization of particles and  
93 release of dissolved organics.

94 The Mediterranean Sea is a prime location for the observation and study of thermohaline  
95 staircases due to its unique hydrographic conditions. The study presented here focuses on the  
96 behaviour of particulate matter and dissolved elements in the Tyrrhenian Sea (Fig. 1), a region  
97 known to be favourable for salt fingers with the formation of large staircases at the transition  
98 between intermediate and deep waters (Durante et al., 2019). The warm and saline Levantine  
99 Intermediate Water (LIW), formed in the eastern Mediterranean Basin, is found throughout the  
100 Tyrrhenian Sea at depths between 200 and 700 m. Deeper is the Tyrrhenian Deep Water  
101 (TDW), colder and less saline, formed by the mixing of the deep waters of the western  
102 Mediterranean with the intermediate and deep waters of the eastern basin Falco et al., 2016).  
103 Staircase structures, which extend over most of the central basin, are found at depths between  
104 600 and 2,500 m and are tens or even hundreds of meters thick.

105 The dataset used in this work was obtained from the PERLE3 cruise (Pujo-Pay et al.,  
106 2020) whose main objective is to study the formation of intermediate Levantine waters in the  
107 eastern basin and their fate and transformation along their course in the Mediterranean Sea.  
108 Here, we focused on a section between the Bay of Naples and southern Sardinia, which cuts the  
109 Tyrrhenian Sea from east to west. The data collected included hydrological parameters  
110 (temperature, salinity, density), hydrodynamic parameters (current velocity and direction), and  
111 particulate (turbidity, large particle abundance) and dissolved (oxygen, nitrate) parameters in  
112 the upper 2000 m of the water column. The two questions addressed here are (1) what are the  
113 characteristics and development conditions of the notable staircase structures observed during  
114 this cruise, and (2) what is the impact of these staircases on the distribution of dissolved and  
115 particulate matter. The answers to these two questions will provide new insights into the  
116 ecological consequences of these small-scale structures.



117 *Figure 1 (a) Map of the stations carried out during part of the PERLE-3 cruise (14–16 March*  
118 *2020) in the Tyrrhenian Sea. Stations 9 and 20, indicated by stars, are the two stations chosen*  
119 *to characterize the water column respectively with and without staircases between intermediate*  
120 *and deep water. (b)  $\theta$ -S diagram for the different stations of the transect and associated water*  
121 *masses (MAW, Modified Atlantic Water; TIW, Tyrrhenian Intermediate Water; LIW, Levantine*  
122 *Intermediate Water; TDW, Tyrrhenian Deep Water).*

123

## 124 **2. Material and Methods**

### 125 **2.1 Shipborne CTD and optical data**

126 This hydrographic survey of the Tyrrhenian Sea was conducted in March 2020 as part of the  
127 PERLE-3 cruise, which was unexpectedly shortened due to the outbreak of the COVID-19  
128 pandemic. It includes 16 stations for which hydrological profiles were obtained between the  
129 surface and 2000 m with a Seabird 911+ CTD-O2 probe. Additional optical sensors (Wetlabs  
130 C-Star 0.25m pathlength transmissometer at 650 nm wavelength, Seabird Suna V2 UV nitrate  
131 sensor, Hydroptic Underwater Vision Profiler (UVP-5) were connected to the probe.

132 Data from the CTD sensors and the transmissometer were recorded at a frequency of  
133 24 Hz. Data were therefore acquired every 2 cm at a descent rate of 1 m/s. The temperature and  
134 conductivity sensors provided measurements with a resolution of 0.0002 °C (4.10<sup>-5</sup> S/m) and  
135 an accuracy of 0.002 °C (0,000 3 S/m), respectively. The dissolved oxygen sensor provided  
136 measurements with a resolution of 0.2 µmol/kg. The transmissometer has a resolution of  
137 1.25 mV over a range of 0 to 5 V (WET Labs, Inc., 2011), giving a beam attenuation coefficient  
138 [BAC=  $-4 \times \ln(T\%)$ , where T% is the transmittance in %] resolution of 10<sup>-3</sup> 1/m. The UVP-5  
139 (Picheral et al., 2010) is a stand-alone instrument mounted on the CTD/rossette frame to quantify  
140 the vertical distribution of large particles and zooplankton. Images are acquired at a frequency  
141 of up to 6 Hz, i.e. on average every 20 cm at a descent rate of 1 m/s. The small size limit of the  
142 UVP-5 is determined by the optical resolution (94.7 µm corresponding to 1 pixel), while the  
143 large size limit is determined by the volume of water illuminated (1.02 l).



144 The stand-alone Seabird Suna V2 UV nitrate sensor attached to the CTD collected data  
145 at 1 Hz from the surface down to 2000 m. It uses ultraviolet absorption spectroscopy to measure  
146 nitrate in situ. A good correlation was observed with bottle measurements over the entire water  
147 column collected during the cruise ( $R^2=0.99$ ,  $N=27$ ,  $p<10^{-5}$ ,  $\text{NO}_3_{\text{SUNA}} = 0.991 \text{NO}_3_{\text{btl}} - 0.116$ ).

148 The CTD data processing was performed with the SBE Data Processing software, and  
149 derived variables (conservative temperature, absolute salinity, potential density anomaly,  
150 Brunt-Väisälä frequency and Turner angle) were estimated based on the TEOS-10 toolbox  
151 (IOC, SCOR and IAPSO, 2010).

152 The transmissometer signal was associated with the finest and most numerous particles  
153 ( $\sim 1\text{--}10 \mu\text{m}$ ), while larger particles (from  $80 \mu\text{m}$ ) were seen by the UVP. For transmissometer  
154 data, the turbidity spikes due to the passage of large particles through the beam were eliminated  
155 by smoothing (Giering et al., 2020). For UVP data, the abundance (in  $\# \text{l}^{-1}$ ) of large particles  
156 for the different size classes between  $80 \mu\text{m}$  and  $2000 \mu\text{m}$  (equivalent circular diameter) was  
157 estimated from the raw images (Picheral et al., 2010). The UVP data were then processed to  
158 estimate the particle size distribution, which was modelled using a typical power law of the  
159 form  $N(d) = C \times d^{-\alpha}$ , where  $C$  represents a constant,  $d$  stands for particle diameter, and  $\alpha$  denotes  
160 the Junge index (Guidi et al., 2009). The Junge index is determined through linear regression  
161 involving log-transformed values of  $N(d)$  and  $d$ . The calculation was performed on the size  
162 range between 80 and 400 microns, in order to consider only the most abundant particles, which  
163 represent to 94% of the total number observed and whose concentration is greater than 1 particle  
164 per litre. The Junge index,  $\alpha$ , varies between 2.5 and 4.5 for this data set. A slope of the  
165 differential particle size distribution of 4 indicates an equal amount of mass in logarithmically  
166 increasing size intervals. Higher values indicate a greater dominance of fine particles within the  
167 particle population, while lower values are associated with particle populations enriched in  
168 larger particles.

169 The filtering step proved to be very important, given the scales on which the study  
170 focused, to remove the spikes and reduce the noise of the signal while maintaining the best  
171 vertical resolution. The 24 Hz raw data were subjected to outlier removal using two successive  
172 moving median filters with window lengths of 7 and 5 scans, respectively. The data were then  
173 binned at 1 m intervals and smoothed with a Loess regression filter. For temperature, salinity,  
174 and potential density anomaly signals, the loess regression smoothing window length was 10  
175 scans (10 metres). For dissolved oxygen, nitrate, beam attenuation coefficient, UVP, and Junge  
176 index signals we applied a Loess regression smoothing with a window length of 50 scan (50  
177 metres).

## 178 2.2 Shipborne acoustical data for current and backscatter index

179 During the PERLE-3 survey, two ship-borne Acoustic Doppler Current Profilers –  
180 ADCPs – collected continuous current data from 21 m to 1200 m depth. The first ADCP was  
181 an RDI OS150 with an acoustic frequency of 150 kHz, a sampling rate of 1 Hz, and a cell size  
182 of 8 m, allowing a total range of 220 m. The second ADCP is an RDI OS38 with an acoustic  
183 frequency of 38 kHz, a sampling rate of 1 Hz, and a cell size of 8 m, allowing a maximum range  
184 of 1200 m. Data averaged over a 2-min period were concatenated and processed using  
185 Cascade V7.2 processing software (Kermabon et al., 2018) to compute horizontal ocean current



186 velocities with a spatial resolution of 2 km, corrected for navigation and ship attitude  
187 parameters, and filtered according to various quality criteria. Bathymetry (Etopo 1) was added  
188 for bottom detection. The profile data for the meridional and zonal components of the current  
189 for the two ADCPs were combined to obtain a complete profile between 21 and 1200 m depth  
190 with maximum resolution in the surface layer.

191 In addition to the S-ADCP current measurements, current data between the surface and  
192 2000 m depth were also collected using a dual-head L-ADCP (Lowered-Acoustic Doppler  
193 Current Profiler) system. These measurements were collected with two RDI  
194 Workhorse 300 kHz current meters mounted on the CTD frame, one looking up and one looking  
195 down. The vertical profiling resolution was 8 m. The data were processed by the velocity  
196 inversion method using version IX of the LDEO software (Thurnherr, 2021). Qualified external  
197 data (CTD, S-ADCP, GPS) are used to process the L-ADCP data. Vertical ocean velocities  
198 were calculated using the LADCP\_w\_ocean utility from combined raw L-ADCP and CTD data  
199 (Thurnherr, 2022). The upward and downward looker data were processed separately and  
200 combined during post-processing to provide vertical velocity profiles for the downcast and  
201 upcast.

202 The data from the S-ADCP were also used to derive the acoustic backscatter index (BI,  
203 Mullison, 2017), which a proxy for the abundance of centimetre-scale reflectors (organic  
204 detritus, zooplankton, micronecton...) in the water column. This derivation takes into account  
205 the absorption and geometric dispersion of sound  $BI = K_C * (RL - Er) + (TL [w] + TL [g])$ , where  
206  $K_C$  is the conversion factor (*count to decibels*) of the ADCP used, RL the received signal, Er  
207 the signal noise, TL [w] and TL [g] are the absorption and geometric dispersion factors of the  
208 acoustic signal in water respectively.

### 209 2.3 Profiling float CTD data

210 Another CTD data set was collected from a BGC profiling float (WMO 6,902,903). This  
211 float is equipped with SBE-41CP pumped CTDs with a sampling rate of 0.5 Hz and an  
212 instrumental precision of 0.01 for salinity, 0.002 °C for temperature and 2.4 dbar for pressure.  
213 CTD profiles are collected during an ascent from the parking depth to the surface, which takes  
214 approximately 3 hours at a nominal vertical speed of 0.1 m/s.

215 The BGC-Argo float collected data for almost 2 years, between 23 June 2018 and 15  
216 March 2020 (date of recovery during the PERLE 3 cruise). It remained in the centre of the  
217 Tyrrhenian Basin (between 39.1-39.7° N, 11.6-12.8° E) during this period. The resulting time  
218 series of CTD profiles includes 16 profiles between 0 and 1000 m from June 23 to July 6, 2018,  
219 and 118 profiles between 0 and 2000 m from July 13, 2018 to March 15, 2020, with a time  
220 resolution of 7 days until October 2019, then 3 days thereafter.

### 221 2.4 Staircases detection

222 Step structures were defined based on temperature and salinity profiles between 500 and  
223 2000 m depth, following the procedure described in Durante et al. (2019). Relative maxima in  
224 the vertical gradient of salinity and potential temperature are used to identify interfaces that  
225 form well-marked steps and delimit a well-mixed layer. Gradient thresholds of 10-4°C/m for  
226 potential temperature and 5 x10-4 PSU/m for salinity were used.



227

228

### 3. Results

229

#### 3.1 Hydrological and hydrodynamical features along the section

230

##### 3.2.1 Temperature, salinity, oxygen, and nitrate

231

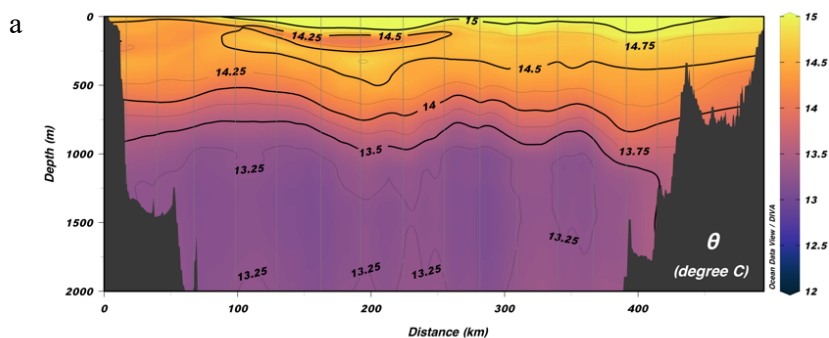
The temperature-salinity diagram (Fig. 1) and the basin cross-section (Fig. 2) clearly identify the distribution of the water masses present in the study area. As in Falco et al. (2016), we used the isohaline 38.72 as the minimum salinity value to identify the shallowest and deepest levels of the LIW. The MAW, which extends in the upper 200 m of the water column, has a higher temperature and lower salinity to the east. To the west, the colder TIW can be distinguished at about 150 m depth. The warmer, saltier, and oxygen-depleted core of the LIW is found at depths between 300 and 600 m. The core of the colder and less salty TDW is visible beyond 1200 m depth.

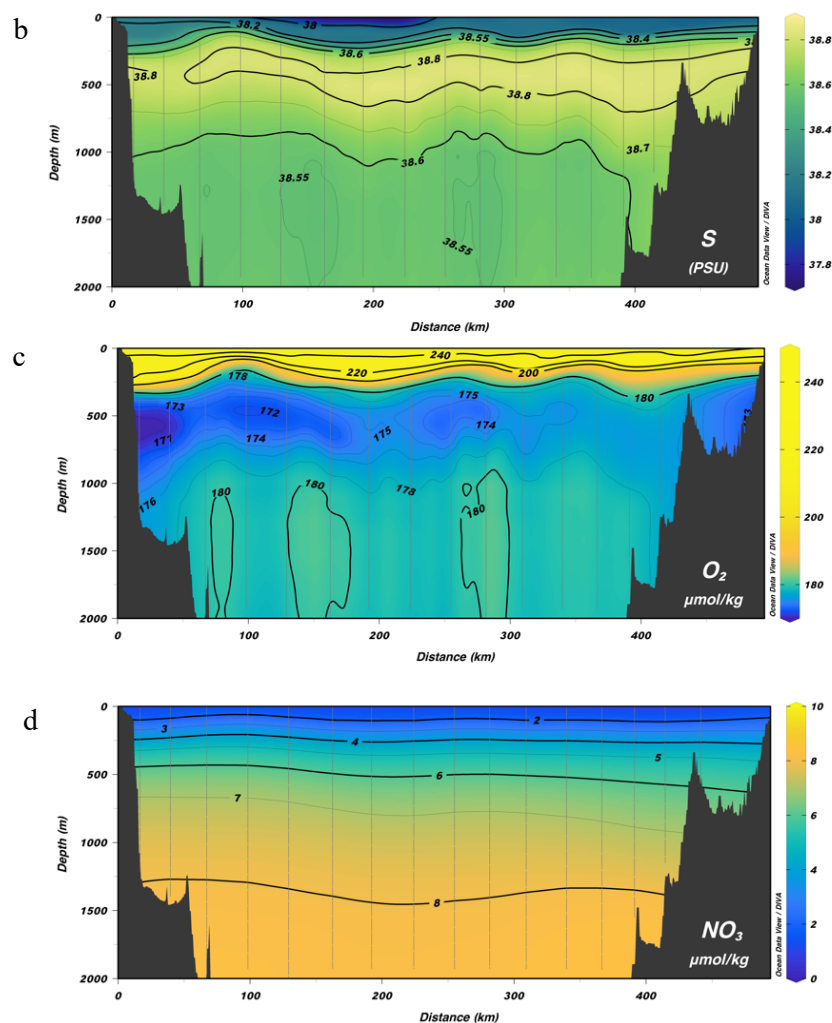
239

240

In March, the nitrate distribution in the Tyrrhenian Sea shows a nutrient-poor surface layer and a nutrient-rich deep layer, typical of oligotrophic conditions. Nitrate concentrations are more stable than the physical parameters, with only small variations across the section. Near the surface, nitrate concentrations are low, about 1  $\mu\text{mol/kg}$ , due to biological uptake. With increasing depth, nitrate concentrations increase. At intermediate depths (250–650 m) they range from 4 to 7  $\mu\text{M}$ , indicating a transition zone with maximum vertical gradients. In deeper waters, concentrations reach 7 to 9  $\mu\text{M}$  due to decomposing organic matter.

247





248 *Figure 2: Cross-basin section of (a) potential temperature, (b) salinity, (c) dissolved oxygen,*  
249 *and (d) nitrates for the PERLE-3 cruise (March 2020).*  
250

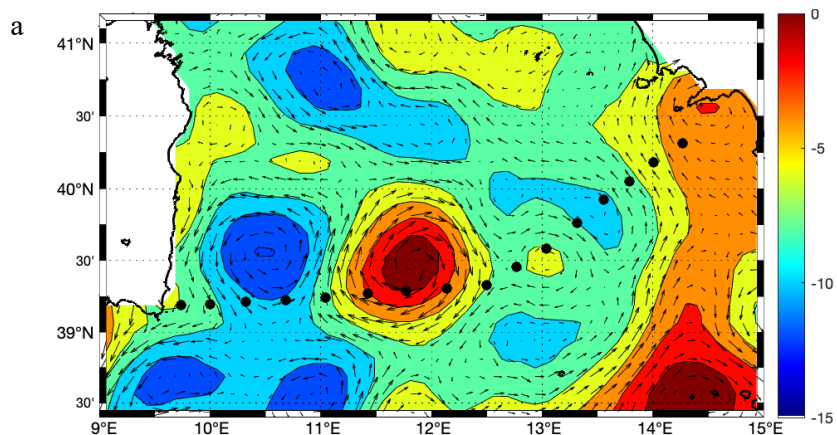
### 251 **3.1.2 Currents**

252 The dynamic topography and currents measured in the water column during PERLE 3  
253 reveal the presence of two large mesoscale eddies in the centre of the basin with maximum  
254 velocities of about  $\sim 30$  cm/s (Fig. 3). The cyclonic eddy at  $10.5^\circ$  E extends to a depth of about  
255 200 m, while the eddy at  $12^\circ$  E extends to more than 500 m. The deep current running along  
256 the eastern edge of the basin defines the general along-slope cyclonic circulation. Below the  
257 LIW core, i.e. at 600 m depth, the currents are very weak, of the order of a few cm/s.

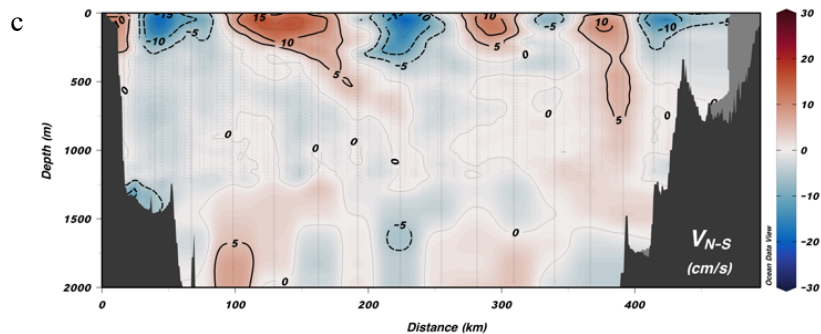
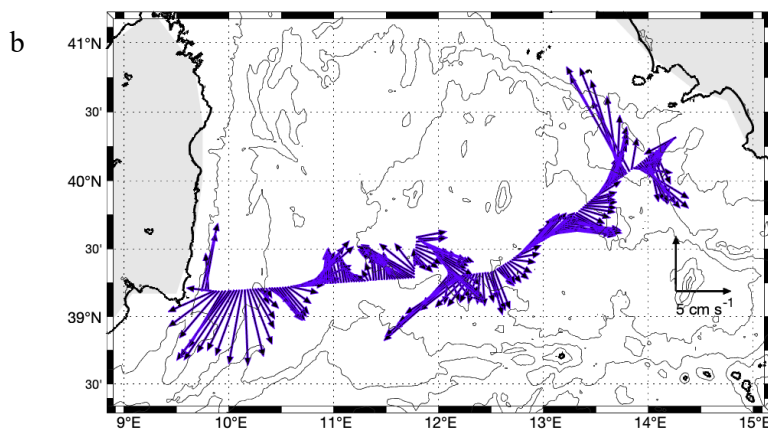




258



259



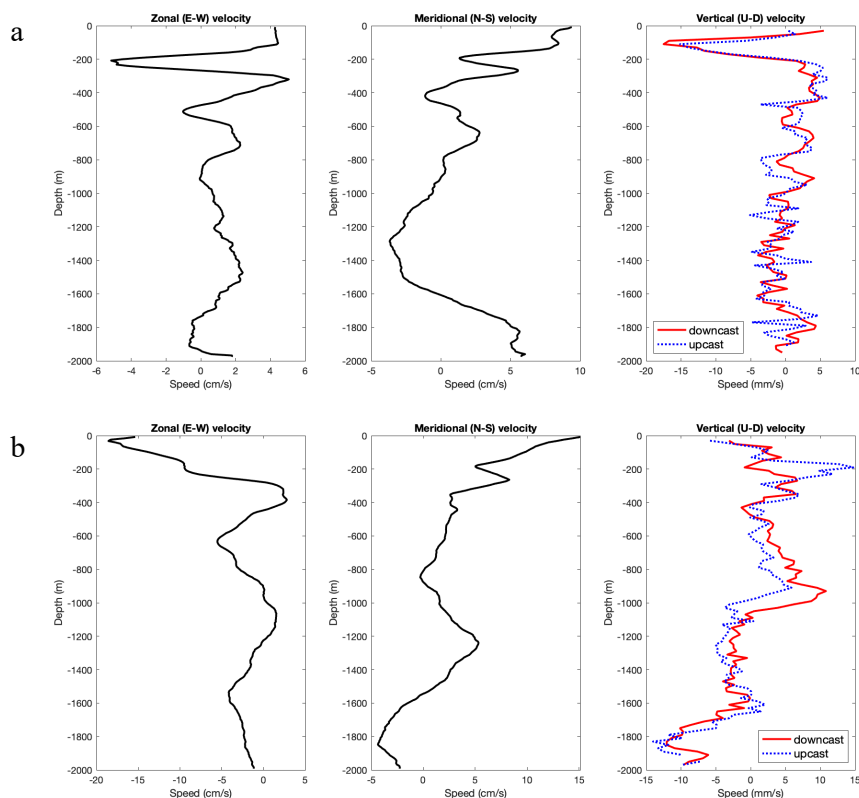
260

261 *Figure 3: (a) Mean absolute dynamic topography during the period of the cruise (14–16 March*  
262 *2020) (b) Stick plot of vertically averaged S-ADCP currents between 21 m and 1200 m along*  
263 *the ship's route across the basin, (c) Meridional component of S-ADCP and L-ADCP currents*  
264 *between the 21 and 2000 m depth for the PERLE-3 cruise.*  
265



266  
267  
268  
269  
270  
271

Later in the text, we'll distinguish between deep stations without significant staircase step structures, such as station 20, and stations with significant staircase steps, such as station 9. In terms of vertical current velocities, the profiles show velocities on the order of mm/s, with standard deviations of a few mm/s, as expected (Fig. 4).



272

273  
274  
275  
276  
277

Figure 4: Vertical profiles of the zonal and meridional components of the horizontal current, and vertical velocities for (a) station 09 and (b) station 20 during the PERLE-3 cruise.

278

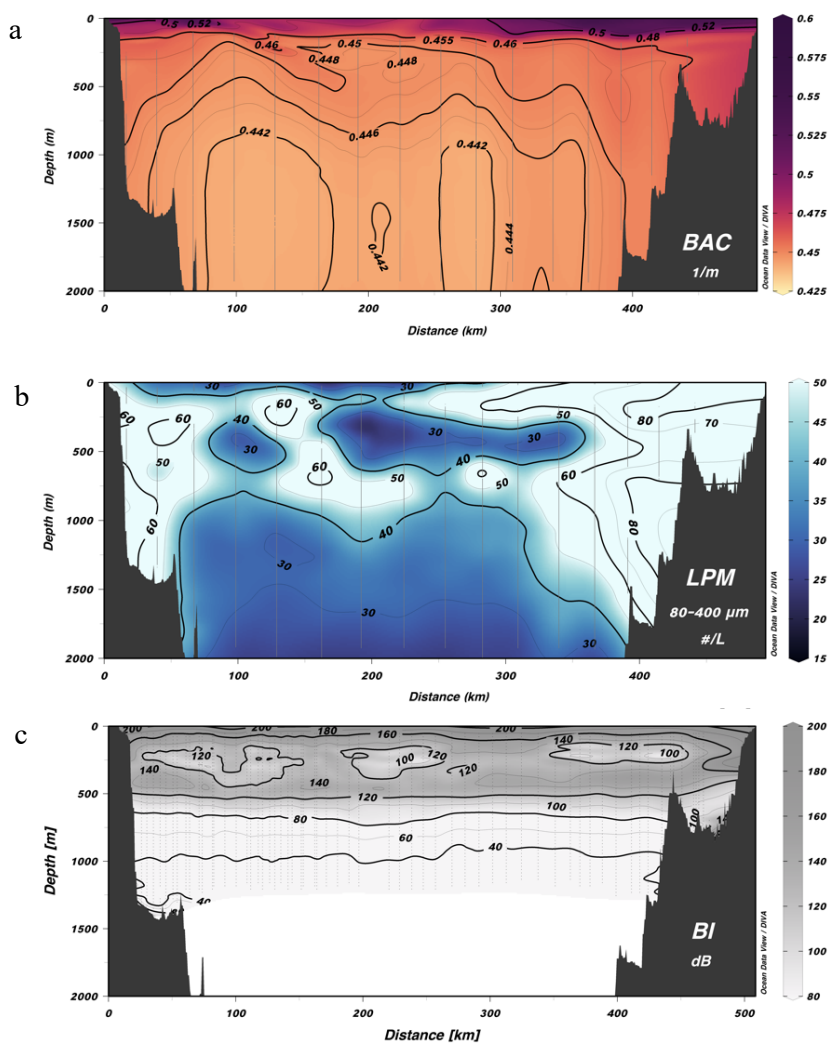
### 3.1.3 Turbidity, large particle abundance and Junge index

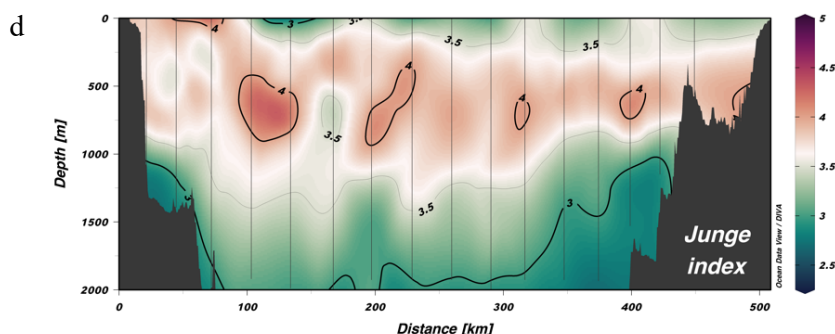
279  
280  
281  
282

The beam attenuation coefficient, an indicator of the abundance of small particles (Fig. 5a) is highest in the surface layer and along the continental slope on both sides of the basin. The tongue of turbid water that descends to 500–600 m in the western half of the basin is associated with the downward movement of water around the anticyclonic eddy.



283 Coarse particles observed with the UVP (Fig. 5b) are most abundant along the  
284 continental slope and between 400 and 900 m depth throughout the basin. The subduction effect  
285 of the anticyclonic eddy is also evident in the abundance of large particles.





286 *Figure 5: Cross-basin section of (a) beam attenuation coefficient, (b) total large particle*  
287 *abundances, (c) backscatter index for the PERLE-3 cruise, and (d) Junge index.*

288 An accumulation of large reflectors between 200 and 500 m depth is clearly visible on  
289 the 38 kHz ADCP echo intensity (Fig. 5c). It corresponds to the deep scattering layer formed  
290 by the micronekton. Its fragmentation is related to the diel vertical migrations of part of the  
291 organisms.

292 The Junge index (Fig. 5d), estimated from UVP data, shows an intermediate maximum –  
293 indicating the preponderance of smaller particles over coarser ones – between 400 and 1000 m,  
294 below the deep scattering layer. Below 1000 m, the index decreases, indicating a relative  
295 decrease in the abundance of smaller particles compared to coarser particles. This decrease is  
296 more pronounced on the continental slope and below deep eddies.

297

## 298 3.2 Hydrological features of thermohaline staircases

### 299 3.2.1 Attributes of staircase station vs. non-staircase station

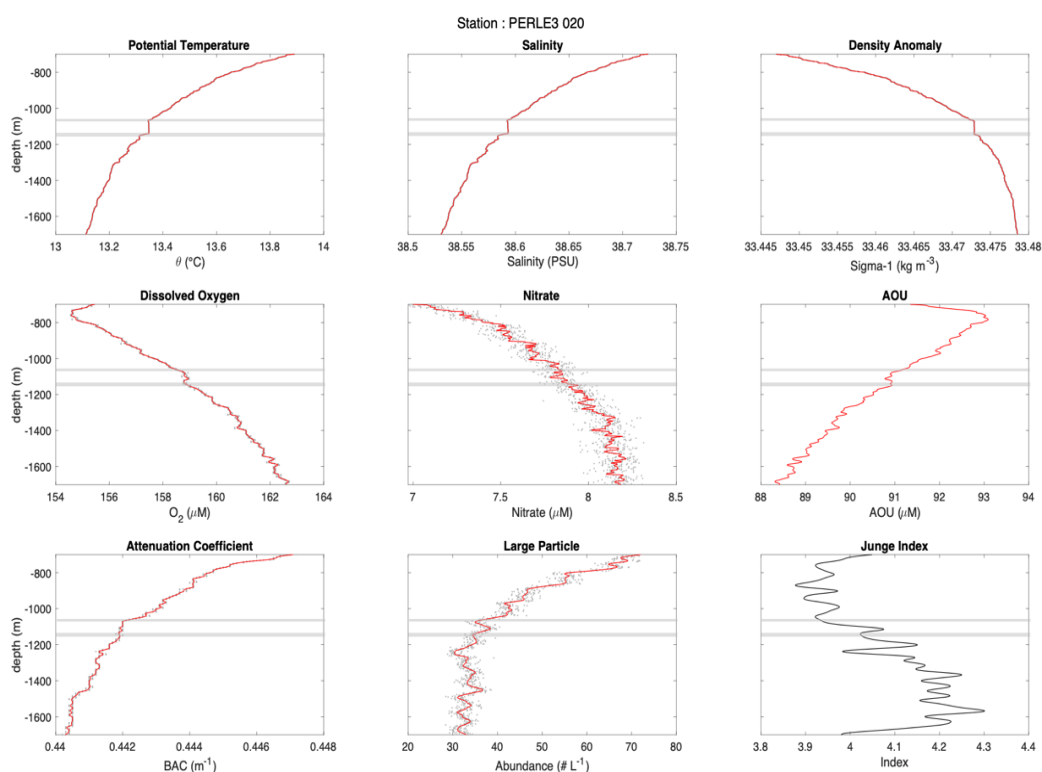
300 In this section we describe the vertical distribution of physical, dissolved and particulate  
301 parameters at station 20, which shows virtually no significant staircase (Fig. 6), and station 09,  
302 which shows marked staircases between 700 and 1700 m (Fig. 7). For all parameters, the  
303 gradients observed at the level of the density steps are small, but significant given the resolution  
304 of the sensors. For most of the variables at station 20, the profiles vary almost uniformly below  
305 800 m depth, with the exception of a homogeneous layer that appears between 1070 and  
306 1140 m, followed by a density step.

307 The profiles of physical variables at station 09 show a series of steps starting at 750 m  
308 depth. Density steps result in thin interfaces (about 9–73 m) and density variations of a few  
309 thousandths of a  $\text{kg}/\text{m}^3$ . The thickness of the mixed layers varies between 10 and 230 m and  
310 increases significantly below 1000 m. The profiles of the biogeochemical variables also show  
311 step-like profiles, with larger gradients corresponding to the density steps and nearly  
312 homogeneous concentrations in the mixed layers between each step. This is clearly visible for  
313 dissolved elements (oxygen, nitrates) and small particle concentration (beam attenuation  
314 coefficient). The effect of the density steps on the abundance of coarser material is less obvious



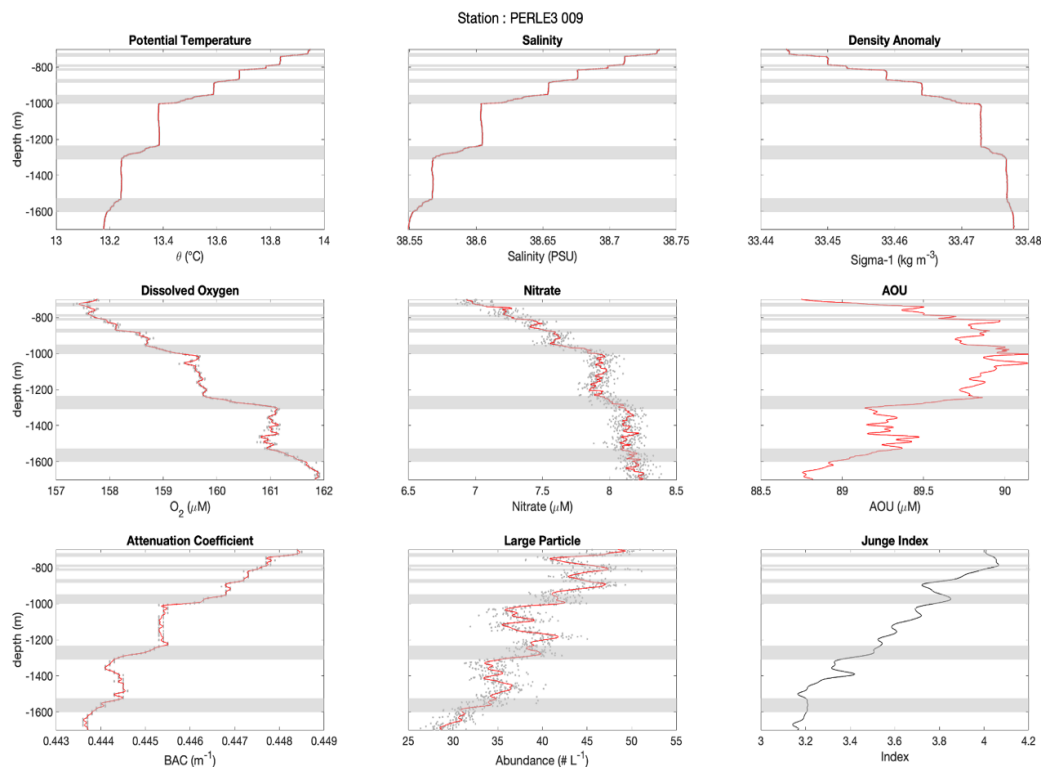
315 due to the variability of the measurements, but it still appears that the total abundance decreases  
316 significantly below each step. It is noteworthy that the decrease in the Junge index between 700  
317 and 1600 m is greater for station 9 with staircase steps, of the order of one unit, than for  
318 station 20, which is more irregular and of the order of 0.2 units.

319



320  
321 *Fig. 6: Profiles of potential temperature, salinity, potential density anomaly (top row) and*  
322 *dissolved oxygen, nitrates, and apparent oxygen utilization (AOU) (middle row), beam*  
323 *attenuation coefficient, large particle abundance between 80 and 400  $\mu\text{m}$ , and Junge index*  
324 *(bottom row) between 700 and 1700 m deep for station PERLE-3\_20. The grey dots are the data*  
325 *binned at 1-metre intervals and the solid red line indicates the smoothed profile. See station*  
326 *position in Fig. 1.*

327



328  
329 *Fig. 7: Profiles of potential temperature, salinity, potential density anomaly (top row) and*  
330 *dissolved oxygen, nitrates, and apparent oxygen utilization (AOU) (middle row), beam*  
331 *attenuation coefficient, large particle abundance between 80 and 400  $\mu\text{m}$ , and Junge index*  
332 *(bottom row) between 700 and 1600 m deep for station PERLE-3\_09. The grey dots are the*  
333 *data binned at 1-metre intervals and the solid red line indicates the smoothed profile. Major*  
334 *density steps are delineated by horizontal grey lines. See station positions in Fig. 1.*

335

### 336 3.2.2 Positioning and persistence of main staircases

337 The transition zone between the LIW and the TDW thus provides the right conditions  
338 (warmer and saltier water mass overlying a colder and less salty water mass) for the double  
339 diffusion phenomenon by salt fingers. The analysis of the thermohaline gradients from the  
340 profiles collected during the cruise and from the profiling float allowed us to identify and  
341 position the main stepped structures in the Tyrrhenian Basin (Fig. 6).

342

343 During the PERLE3 cruise, the staircases develop clearly between 600 and 2000 m  
344 depth, mostly in the centre of the basin (Fig. 8a). Staircases are absent under the deepest eddy

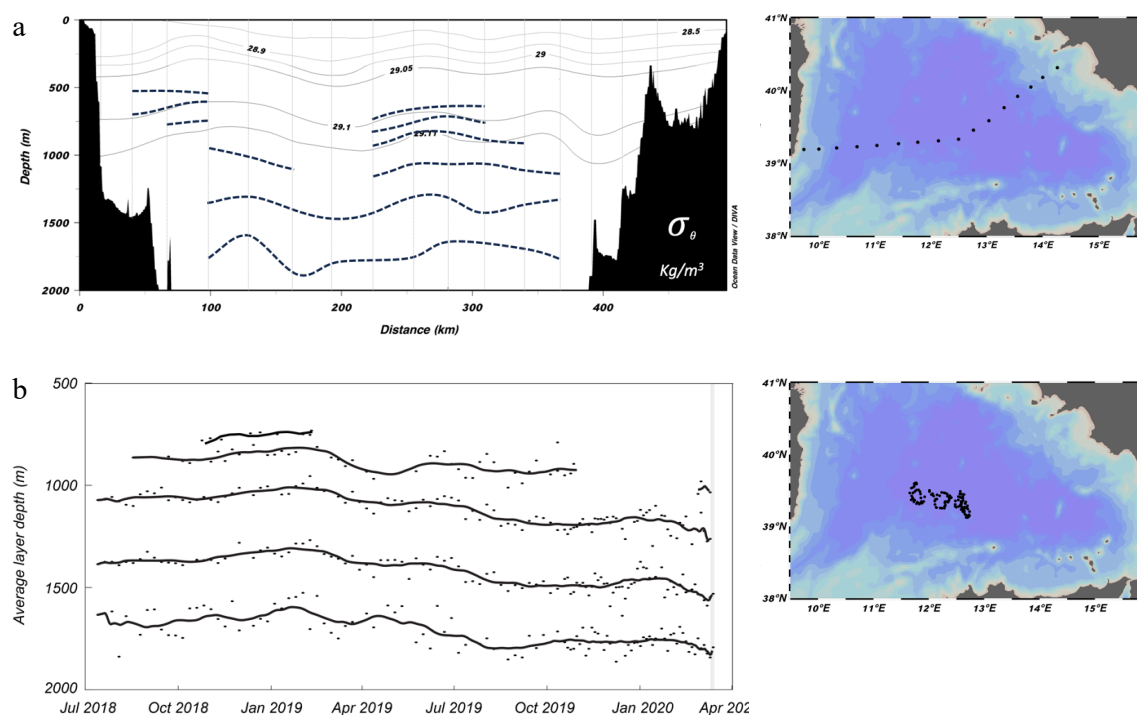


345 (about 12° E). Staircases are absent near the western slope and below the anticyclonic eddy at  
346 about 12° E down to 1000 m depth.

347

348 The temporal evolution of the staircase in the centre of the basin, as seen by the profiling  
349 float between July 2018 and March 2020, underscores that these structures, particularly at  
350 depths greater than 1000 m, are relatively stable and have been maintained for several years  
351 (Fig. 8b).

352



353

354 *Figure 8: (a) depth of the main thermohaline staircases across the basin during the PERLE3*  
355 *cruise and (b) temporal evolution of the staircases in the centre of the basin as seen by the*  
356 *profiling float between July 2018 and March 2020. The shaded band indicates the campaign*  
357 *period. The position of the stations and the trajectory of the profiling float are shown on the*  
358 *maps on the right.*

359

## 360 4. Discussion

### 361 4.1 Characteristics and development conditions of the notable staircase



362 A large part of the oceanic regions are suitable for the process of double diffusion and  
363 salt fingering, but it clearly develops only in some of them, especially in the Mediterranean.  
364 Meccia et al. (2016) have shown that about 50% of the Mediterranean Sea is favourable for  
365 double diffusion processes, with the Tyrrhenian, Ionian, and southwestern Mediterranean  
366 basins being most susceptible to salt fingering, and the strongest processes potentially occurring  
367 in the deep waters of the Tyrrhenian Sea.

368 Our observations in the Tyrrhenian Sea between the surface and 2000 m show some  
369 well-defined thermohaline staircase structures associated with salt fingers, while observations  
370 made during the PERLE cruises in the Ionian Sea and Levantine Basin do not show any  
371 particulate structures associated with salt fingers. The observed thermohaline staircases occur  
372 mainly in the centre of the Tyrrhenian Basin and are less defined on the continental slope at  
373 both ends of the section. These latter regions are the ones that contain the cyclonic boundary  
374 circulation that entrains the core of the LIWs originating from the Strait of Sicily. These results  
375 are consistent with those of Zodiatis and Gasparini (1996) from ship observations, of Buffett et  
376 al. (2017) from seismic observations, and Taillandier et al. (2020) from profiling float  
377 observations, who showed that the staircases with the most distinct step-like gradients appear  
378 in the centre of the basin, while they become more diffuse towards the boundaries and the  
379 bottom. They linked this change to increased vertical motions that prevent diffuse convection  
380 and staircase formation because the internal wave field and current shear are stronger near the  
381 boundaries.

382 Durante et al. (2021) suggested that mixing induced by internal gravitational waves can  
383 modulate the staircase structure. Our observations show that the presence of significant  
384 staircase structures down to 2000 m can also be influenced by mixing induced by cyclonic  
385 eddies present in the basin. When the vertical extent of these eddies reaches depths deeper than  
386 the LIW (i.e. about 500 m), the intensity and variability of the currents in the transition zone  
387 between the LIW and the TDW visibly alter the development of the staircases. These  
388 observations confirm that, even within the basin, step structures appear to develop preferentially  
389 in areas of weak horizontal and vertical currents. However, the modification by eddies would  
390 be episodic and would hardly affect the lower part of the salt finger region, as several studies  
391 show that the central Tyrrhenian thermohaline steps observed in the heart of the basin interior  
392 are quite stable and can persist for years (Taillandier et al., 2020) to decades (Durante et al.,  
393 2019).

394

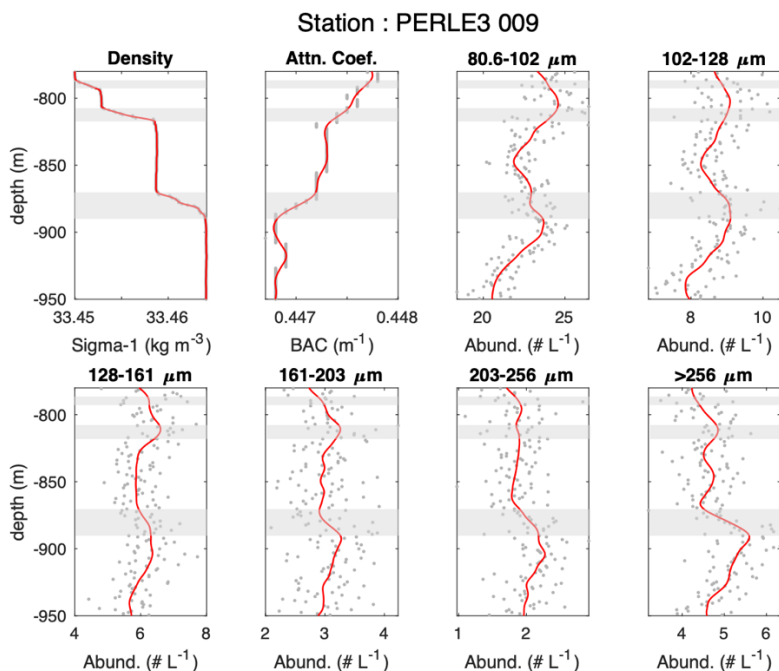
#### 395 **4.2 Impact of staircases on the distribution and settling of particulate matter**

396 The effect of density steps on the vertical distribution of particle abundance is detailed  
397 for three interfaces between 790 m and 950 m (Fig. 9) and one larger interface between 1150  
398 and 1400 m (Fig. 10). Both examples show a significant reduction in the abundance of fine  
399 particles as seen by transmissometry (BAC) under each interface. For large particles seen by  
400 the UVP, the evolution of abundance on either side of the interface differs depending on size.  
401 For the smallest size ranges (80.6-128  $\mu\text{m}$ ) the abundance decreases slightly whereas for larger  
402 size ranges it hardly varies and, in some cases, even increases. This evolution with depth  
403 indicates that at each density interface, there is likely to be a retention of some of the finer  
404 particles, as well as coarser ones whose effective density is close to that of ambient water. The



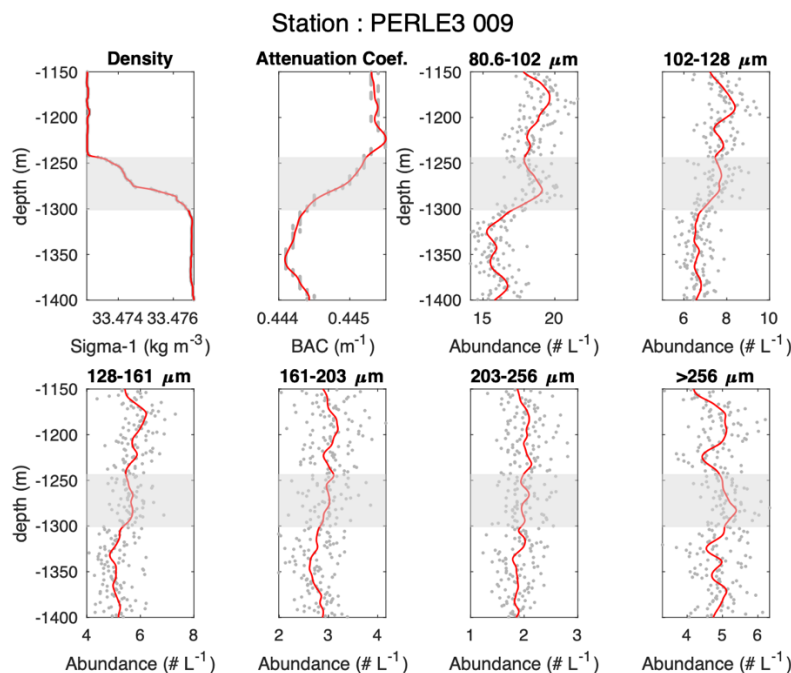


405 larger particles, which are generally denser and have higher settling velocities, are not affected  
406 by the change in water density.



408 *Figure 9: Profiles of potential density anomaly, beam attenuation coefficient, large particle*  
409 *abundances for the first four size classes and for all sizes >256 μm of the UVP between 780*  
410 *and 950 m deep for station PERLE3-09. Grey stripes identify the main steps in density.*

411



413 *Figure 10: Profiles of potential density anomaly, beam attenuation coefficient, large particle*  
414 *abundances for the first four size classes and for all sizes >256  $\mu\text{m}$  of the UVP between 1150*  
415 *and 1400 m deep for station PERLE3-09. Grey stripes identify the main steps in density.*  
416

417 The slope of the Junge-type particle size spectrum has been shown to be a valid first-  
418 order description of the particle size distribution, particularly for the study of size-dependent  
419 processes such as particle sinking (Guidi et al., 2009). In our case, the observed abundance of  
420 coarse particles and the slope of the particle size spectrum are greatest in the deep scattering  
421 layer between 400 and 800 m (Fig. 5). Deeper down to 2000 m, both the total particle  
422 abundance and the slope of the size spectrum decrease, indicating that the contribution of  
423 coarser particles to the particle population increases with depth. Similar results regarding the  
424 size distribution of smaller particles in the Tyrrhenian Basin were obtained by Chaikalis et al.  
425 (2021) during the trans-Mediterranean cruise in March 2018 using an in-situ laser scattering  
426 and transmissometry instrument (LISST-Deep). In this study, they considered the size range  
427 between 5.6 and 92.6  $\mu\text{m}$ , complementary to that measured with the UVP. Their stations show  
428 similar profiles of the particle size spectrum below the surface layer (>150 m), with an  
429 intermediate maximum at about 400–500 m depth and a steady decrease to 2000 m depth. Such  
430 an evolution of the abundance and particle size spectra is generally considered to be the result  
431 of aggregation, with smaller particles agglomerating to form larger ones, a common process in  
432 the ocean (McCave, 1984).

433 Based on laboratory and modelling experiments in the literature, strong density  
434 interfaces are known to cause particle retention and promote aggregation. According to



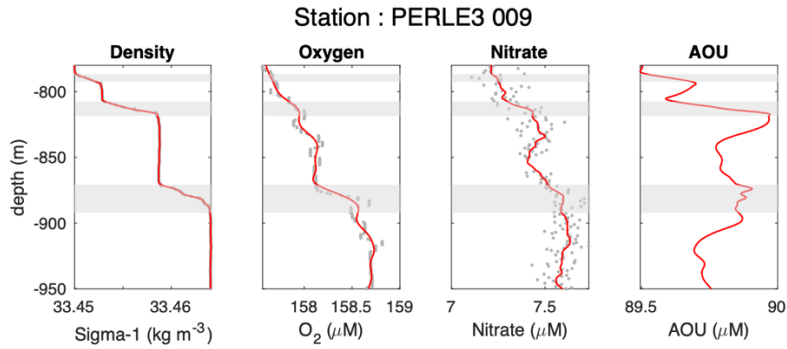
435 Doostmohammadi and Ardekani (2015), density interfaces can induce preferential retention of  
436 fine, slow-sinking particles compared to larger particles, and can therefore promote the  
437 formation of clusters of fine particles, which can then aggregate. This retention phenomenon  
438 can also act on coarse particles, which are often formed by high porosity aggregates. According  
439 to Kindler et al. (2010), large porous particles are much more dependent on transition zones  
440 and large accumulations of porous particles can occur at interfaces due to their less dense water  
441 transport, which is also conducive to aggregation. In our case, the staircase density interfaces  
442 are really weak (a few thousandths of kg/m<sup>3</sup>) and despite the measurement uncertainty of the  
443 particle abundances, the results suggest that these interfaces have an effect on the size  
444 distribution – through aggregation – of the settling particles.

445 In addition, convection phenomena in the mixed layers sandwiching the density  
446 interfaces are likely to even out the concentration of slowly sinking particles (especially the  
447 finest and most numerous). The vertical velocities of the current measured, at  $\pm$ a few mm/s, are  
448 likely to alter the settling of particles, helping to equalise their abundance and increase their  
449 residence time in each layer.

450

#### 451 **4.3 Potential impact of staircases on the biogeochemical activity**

452 At station 20 (fig. 6), the lack of staircase structures and density interfaces results in  
453 relatively uniform sedimentation of particulate matter and relatively homogeneous biogeo-  
454 chemical processes throughout the water column. As particles descend into the deep ocean, they  
455 undergo a progressive but overall constant mineralization process by bacteria (Ghiglione et al.,  
456 2009). In contrast, stations with staircase structures show distinct layered profiles for dissolved  
457 oxygen and nitrate (figs. 10 and 11). These staircases facilitate the retention and aggregation of  
458 sinking particulate matter, which is critical for the mineralization and transformation of organic  
459 matter in the water column (Wakeham and Lee, 1993). This remineralization process releases  
460 additional nutrients and consumes oxygen, potentially leading to localized oxygen depletion or  
461 an increase in Apparent Oxygen Utilization (AOU), particularly evident in the shallow stair-  
462 cases between 750 and 900 m at station 9 (Fig. 11). At the deeper interface around 1300 m  
463 (Fig. 12), the increase in AOU may be masked by a stronger vertical oxygen gradient. These  
464 interfaces are thought to create specific microenvironments that influence microbial community  
465 composition and local biological productivity, similar to the concept of plastispheres described  
466 by Conan et al. (2022). Consequently, the formation of distinct layers allows various organisms  
467 to colonize specific microhabitats, thereby enhancing biodiversity and trophic interactions.

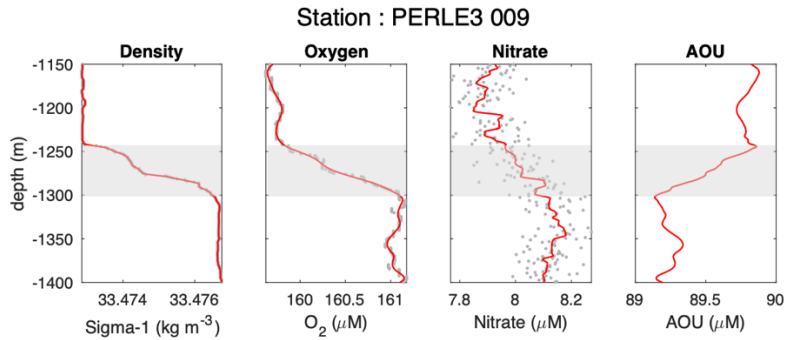


468

469 *Figure 11: Profiles of potential density anomaly, dissolved oxygen, nitrates and Apparent*  
 470 *Oxygen Utilization (AOU) between 780 and 950 m deep for station PERLE3-09. Grey stripes*  
 471 *identify the main steps in density.*

472

473



474

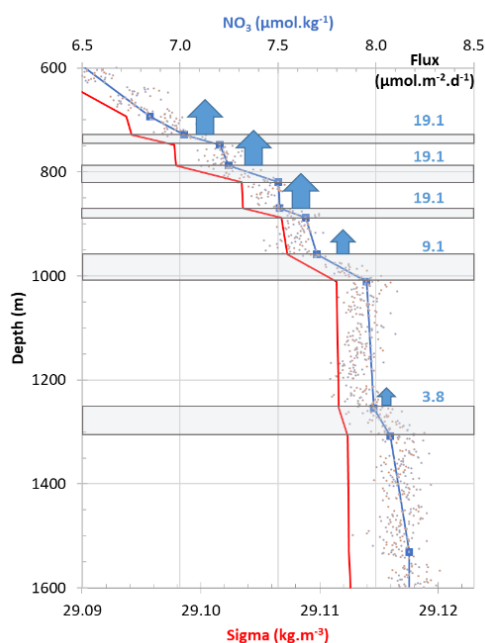
475 *Figure 12: Profiles of potential density anomaly, dissolved oxygen, nitrates and Apparent*  
 476 *Oxygen Utilization (AOU) between 1150 and 1400 m deep for station PERLE3-09. Grey stripes*  
 477 *identify the main steps in density.*

478 Taillandier et al. (2020) showed that the thermohaline staircases in the Tyrrhenian Sea  
 479 significantly influence the biogeochemical dynamics by contributing to the nitrate enrichment  
 480 of the LIW through diffusion. They estimated upward nitrate fluxes in the transition zone be-  
 481 tween 400 and 2000 m depth to be about  $4 \mu\text{mol}/\text{m}^2/\text{d}$  using the salt diffusivity formulation of  
 482 Radko and Smith (2012) based on the density ratio ( $R\rho = -\alpha \cdot \partial\theta/\partial z - \beta \cdot \partial S/\partial z$ ), where  $\alpha$  and  
 483  $\beta$  are the thermal expansion and haline contraction coefficients of seawater, respectively, and  
 484 the molecular diffusivity of heat is  $k_T = 1.4 \times 10^{-7} \text{ m}^2/\text{s}$ . Based on this study, we calculated  
 485 nitrate fluxes at each interface using the same formulation. The nitrate flux can be expressed  
 486 as:

487 
$$F_{\text{NO}_3} = K_{\text{sf}} \cdot \partial C_{\text{NO}_3} / \partial z = k_T \cdot R_\rho \cdot (135.7 / (R_\rho - 1)^{1/2} - 62.75) \cdot \partial C_{\text{NO}_3} / \partial z$$



488 At station 9, the diffusive nitrate flux was assessed for each depth step between 600 and  
489 1600 m (Fig. 13). Fluxes ranged from 3.8  $\mu\text{mol}/\text{m}^2/\text{d}$  at the deepest depth (1254 m) to  
490 19.1  $\mu\text{mol}/\text{m}^2/\text{d}$  for the three shallower depths (728 to 870 m). The fluxes at the interfaces are  
491 therefore stronger than the overall flux estimated by Taillandier et al. (2020) for the 400–2000  
492 m depth range. Fluxes at interfaces are the major contributor to the total nitrate flux. It is conceivable  
493 that the release of additional nutrients at the upper interfaces increases the local vertical  
494 gradient, thereby enhancing diffusive fluxes.



495

496 *Figure 13: Estimated diffusive fluxes of nitrate (in  $\mu\text{mol}/\text{m}^2/\text{d}$ ) from station 9 at the interfaces*  
497 *of each gradient zone characterizing a staircase step. In red: the vertical profile of the specific*  
498 *volume anomaly ( $\sigma_\theta$  in  $\text{kg}/\text{m}^3$ ) delimiting homogeneous and gradient zones. The grey points*  
499 *correspond to nitrate measurements by the SUNA, while the blue squares are the values*  
500 *averaged over 1 m for each point at the upper and lower interfaces, making it possible to*  
501 *calculate the nitrate gradient in the shaded areas.*

502

## 503 **5. Conclusion**

504 This study examines observations of the effect of weakly stepped density gradients  
505 induced by salt fingering phenomena on the distribution and fluxes of particulate and dissolved  
506 elements. While the effect of density steps on particle settling has been well studied  
507 experimentally and demonstrated for strong density gradients in natural environments (i.e.  
508 buoyant river plumes and pycnocline), this is the first time, to our knowledge, that this effect



509 has been identified for steps with the extremely low density gradients that exist in the deep  
510 ocean.

511 In the Tyrrhenian Sea, the interface between the warm and saline intermediate waters  
512 (LIW) and the colder and less saline deep waters (TDW) presents thermohaline conditions  
513 favourable to the development of significant salt fingering staircases. Profiles with mixed layers  
514 tens to hundreds of metres thick and density steps of a few thousandths of  $\text{kg/m}^3$  occur in zones  
515 of low hydrodynamic energy, away from strong horizontal currents, such as near the  
516 boundaries. The study also shows that these steps are mostly stable and persist for years,  
517 especially in the central basin, while they are disrupted or absent in regions with stronger  
518 hydrodynamics, such as near deep-reaching eddies.

519 The presence of thermohaline staircases appears to significantly influence the  
520 distribution of particulate and dissolved matter. Profiles of particle abundance down to a few  
521 hundred microns, or profiles of dissolved substances such as oxygen and nitrates, tend to follow  
522 that of density, i.e. show staircases in areas affected by salt finger mixing processes, or vary  
523 regularly in unaffected areas.

524 The density steps caused by these staircases modify the particle size distribution, leading  
525 to an evolution towards larger aggregates. In fact, the retention of near-floating particles at  
526 density interfaces increases their residence time, promotes particle aggregation and,  
527 incidentally, allows the larger particles thus formed to cross the density interface, with possible  
528 implications for the vertical flux of carbon.

529 The staircases influence the concentration of nutrients (such as nitrates) and dissolved  
530 oxygen levels, thereby influencing the biogeochemical cycling within these layers. The  
531 retention of part of the particulate material at the density interfaces allows the mineralization of  
532 organic matter, the effect of which on oxygen and nitrate concentrations is superimposed on the  
533 upward flux by diapycnal diffusion. Ecologically, it is hypothesized that these staircases may  
534 play a crucial role in promoting diverse habitats and influencing the lability of organic matter  
535 and nutrient distribution.

536

## 537 **References**

538 Buffett, G.G., Krahnemann, G., Klaeschen, D., Schroeder, K., Sallarès, V., Papenberg, C., Ranero,  
539 C.R., Zitellini, N., 2017. Seismic Oceanography in the Tyrrhenian Sea: Thermohaline  
540 Staircases, Eddies, and Internal Waves. *JGR Oceans* 122, 8503–8523.  
541 <https://doi.org/10.1002/2017JC012726>

542 Chaikalas, S., Parinos, C., Möbius, J., Gogou, A., Velaoras, D., Hainbucher, D., Sofianos, S.,  
543 Tanhua, T., Cardin, V., Proestakis, E., Amiridis, V., Androni, A., Karageorgis, A., 2021.  
544 Optical Properties and Biochemical Indices of Marine Particles in the Open Mediterranean Sea:  
545 The R/V Maria S. Merian Cruise, March 2018. *Front. Earth Sci.* 9, 614703.  
546 <https://doi.org/10.3389/feart.2021.614703>

547 Conan, P., Philip, L., Ortega-Retuerta, E., Odobel, C., Duran, C., Pandin, C., Giraud, C.,



- 548 Meistertzheim, A.-L., Barbe, V., Ter Hall, A., Pujo-Pay, M., Ghiglione, J.-F., 2022. Evidence  
549 of coupled autotrophy and heterotrophy on plastic biofilms and its influence on surrounding  
550 seawater. *Environmental Pollution* 315, 120463. <https://doi.org/10.1016/j.envpol.2022.120463>
- 551 Davarpanah Jazi, S., Wells, M.G., 2016. Enhanced sedimentation beneath particle-laden flows  
552 in lakes and the ocean due to double-diffusive convection. *Geophysical Research Letters* 43.  
553 <https://doi.org/10.1002/2016GL069547>
- 554 Doostmohammadi, A., Ardekani, A.M., 2015. Suspension of solid particles in a density  
555 stratified fluid. *Physics of Fluids* 27, 023302. <https://doi.org/10.1063/1.4907875>
- 556 Doostmohammadi, A., Ardekani, A.M., 2014. Reorientation of elongated particles at density  
557 interfaces. *Phys. Rev. E* 90, 033013. <https://doi.org/10.1103/PhysRevE.90.033013>
- 558 Durante, S., Oliveri, P., Nair, R., Sparnocchia, S., 2021. Mixing in the Tyrrhenian Interior Due  
559 to Thermohaline Staircases. *Front. Mar. Sci.* 8, 672437.  
560 <https://doi.org/10.3389/fmars.2021.672437>
- 561 Durante, S., Schroeder, K., Mazzei, L., Pierini, S., Borghini, M., Sparnocchia, S., 2019.  
562 Permanent Thermohaline Staircases in the Tyrrhenian Sea. *Geophysical Research Letters* 46,  
563 1562–1570. <https://doi.org/10.1029/2018GL081747>
- 564 Falco, P., Trani, M., Zambianchi, E., 2016. Water mass structure and deep mixing processes in  
565 the Tyrrhenian Sea: Results from the VECTOR project. *Deep Sea Research Part I: Oceanographic Research Papers* 113, 7–21. <https://doi.org/10.1016/j.dsr.2016.04.002>
- 567 Ghiglione, J.-F., Conan, P., Pujo-Pay, M., 2009. Diversity of total and active free-living vs.  
568 particle-attached bacteria in the euphotic zone of the NW Mediterranean Sea. *FEMS*  
569 *Microbiology Letters* 299, 9–21. <https://doi.org/10.1111/j.1574-6968.2009.01694.x>
- 570 Giering, S.L.C., Cavan, E.L., Basedow, S.L., Briggs, N., Burd, A.B., Darroch, L.J., Guidi, L.,  
571 Irisson, J.-O., Iversen, M.H., Kiko, R., Lindsay, D., Marcolin, C.R., McDonnell, A.M.P.,  
572 Möller, K.O., Passow, U., Thomalla, S., Trull, T.W., Waite, A.M., 2020. Sinking Organic  
573 Particles in the Ocean—Flux Estimates From in situ Optical Devices. *Front. Mar. Sci.* 6, 834.  
574 <https://doi.org/10.3389/fmars.2019.00834>
- 575 Green, T., 1987. The importance of double diffusion to the settling of suspended material.  
576 *Sedimentology* 34, 319–331. <https://doi.org/10.1111/j.1365-3091.1987.tb00780.x>
- 577 Guidi, L., Stemann, L., Jackson, G.A., Ibanez, F., Claustre, H., Legendre, L., Picheral, M.,  
578 Gorsky, G., 2009. Effects of phytoplankton community on production, size, and export of large  
579 aggregates: A world-ocean analysis. *Limnology & Oceanography* 54, 1951–1963.  
580 <https://doi.org/10.4319/lo.2009.54.6.1951>
- 581 Hoshiba, Y., Hasumi, H., Itoh, S., Matsumura, Y., Nakada, S., 2021. Biogeochemical impacts  
582 of flooding discharge with high suspended sediment on coastal seas: a modeling study for a  
583 microtidal open bay. *Sci Rep* 11, 21322. <https://doi.org/10.1038/s41598-021-00633-8>
- 584 Hoyal, D.C.J.D., Bursik, M.I., Atkinson, J.F., 1999. The influence of diffusive convection on



- 585 sedimentation from buoyant plumes. *Marine Geology* 159, 205–220.  
586 [https://doi.org/10.1016/S0025-3227\(99\)00005-5](https://doi.org/10.1016/S0025-3227(99)00005-5)
- 587 IOC, SCOR and IAPSO, 2010. The international thermodynamic equation of seawater – 2010:  
588 Calculation and use of thermodynamic properties.
- 589 Kermabon, C., Lherminier, P., Le Bot, P., Gaillard, F., 2018. Chaîne Automatisée de Suivi des  
590 Courantomètres Acoustiques Doppler Embarqués - Cascade V7.2: Logiciel de validation et de  
591 visualisation des mesures ADCP de coque.
- 592 Kiko, R., Picheral, M., Antoine, D., Babin, M., Berline, L., Biard, T., Boss, E., Brandt, P.,  
593 Carlotti, F., Christiansen, S., Coppola, L., De La Cruz, L., Diamond-Riquier, E., Durrieu De  
594 Madron, X., Elineau, A., Gorsky, G., Guidi, L., Hauss, H., Irisson, J.-O., Karp-Boss, L.,  
595 Karstensen, J., Kim, D., Lekanoff, R.M., Lombard, F., Lopes, R.M., Marec, C., McDonnell,  
596 A.M.P., Niemeyer, D., Noyon, M., O'Daly, S.H., Ohman, M.D., Pretty, J.L., Rogge, A.,  
597 Searson, S., Shibata, M., Tanaka, Y., Tanhua, T., Taucher, J., Trudnowska, E., Turner, J.S.,  
598 Waite, A., Stemann, L., 2022. A global marine particle size distribution dataset obtained with  
599 the Underwater Vision Profiler 5. *Earth Syst. Sci. Data* 14, 4315–4337.  
600 <https://doi.org/10.5194/essd-14-4315-2022>
- 601 Kindler, K., Khalili, A., Stocker, R., 2010. Diffusion-limited retention of porous particles at  
602 density interfaces. *Proc. Natl. Acad. Sci. U.S.A.* 107, 22163–22168.  
603 <https://doi.org/10.1073/pnas.1012319108>
- 604 Maggi, F., 2013. The settling velocity of mineral, biomineral, and biological particles and  
605 aggregates in water: SPM SETTLING VELOCITY IN WATER. *J. Geophys. Res. Oceans* 118,  
606 2118–2132. <https://doi.org/10.1002/jgrc.20086>
- 607 McCave, I.N., 1984. Size spectra and aggregation of suspended particles in the deep ocean.  
608 *Deep Sea Research Part A. Oceanographic Research Papers* 31, 329–352.  
609 [https://doi.org/10.1016/0198-0149\(84\)90088-8](https://doi.org/10.1016/0198-0149(84)90088-8)
- 610 McCave, I.N., 1975. Vertical flux of particles in the ocean. *Deep Sea Research and*  
611 *Oceanographic Abstracts* 22, 491–502. [https://doi.org/10.1016/0011-7471\(75\)90022-4](https://doi.org/10.1016/0011-7471(75)90022-4)
- 612 Meccia, V.L., Simoncelli, S., Sparnocchia, S., 2016. Decadal variability of the Turner Angle in  
613 the Mediterranean Sea and its implications for double diffusion. *Deep Sea Research Part I:*  
614 *Oceanographic Research Papers* 114, 64–77. <https://doi.org/10.1016/j.dsr.2016.04.001>
- 615 Millot, C., Taupier-Letage, I., 2005. Circulation in the Mediterranean Sea, in: Saliot, A. (Ed.),  
616 *The Mediterranean Sea, Handbook of Environmental Chemistry*. Springer Berlin Heidelberg,  
617 Berlin, Heidelberg, pp. 29–66. <https://doi.org/10.1007/b107143>
- 618 Mrokowska, M.M., 2018. Stratification-induced reorientation of disk settling through ambient  
619 density transition. *Sci Rep* 8, 412. <https://doi.org/10.1038/s41598-017-18654-7>
- 620 Mullison, J., 2017. Backscatter Estimation Using Broadband Acoustic Doppler Current  
621 Profilers-Updated.





- 622 Newton, P.P., Liss, P.S., 1990. Particles in the oceans (and other natural waters). *Science*  
623 *Progress* (1933- ) 74, 91–114.
- 624 Omand, M.M., Govindarajan, R., He, J., Mahadevan, A., 2020. Sinking flux of particulate  
625 organic matter in the oceans: Sensitivity to particle characteristics. *Sci Rep* 10, 5582.  
626 <https://doi.org/10.1038/s41598-020-60424-5>
- 627 Parsons, J.D., Garcia, M.H., 2000. Enhanced Sediment Scavenging Due to Double-Diffusive  
628 Convection. *Journal of Sedimentary Research* 70, 47–52. [https://doi.org/10.1306/2DC408FD-](https://doi.org/10.1306/2DC408FD-0E47-11D7-8643000102C1865D)  
629 [0E47-11D7-8643000102C1865D](https://doi.org/10.1306/2DC408FD-0E47-11D7-8643000102C1865D)
- 630 Picheral, M., Guidi, L., Stemmann, L., Karl, D.M., Iddaoud, G., Gorsky, G., 2010. The  
631 Underwater Vision Profiler 5: An advanced instrument for high spatial resolution studies of  
632 particle size spectra and zooplankton. *Limnology & Ocean Methods* 8, 462–473.  
633 <https://doi.org/10.4319/lom.2010.8.462>
- 634 Prairie, J., Ziervogel, K., Arnosti, C., Camassa, R., Falcon, C., Khatri, S., McLaughlin, R.,  
635 White, B., Yu, S., 2013. Delayed settling of marine snow at sharp density transitions driven by  
636 fluid entrainment and diffusion-limited retention. *Mar. Ecol. Prog. Ser.* 487, 185–200.  
637 <https://doi.org/10.3354/meps10387>
- 638 Pujo-Pay M., Durrieu de Madron X., Conan P., 2020. PERLE3 cruise, Pourquoi Pas ? R/V.  
639 <https://doi.org/10.17600/18001342>
- 640 Radko, T., 2013. *Double-diffusive convection*. Cambridge university press, Cambridge.
- 641 Radko, T., Smith, D.P., 2012. Equilibrium transport in double-diffusive convection. *J. Fluid*  
642 *Mech.* 692, 5–27. <https://doi.org/10.1017/jfm.2011.343>
- 643 Taillandier, V., Prieur, L., D’Ortenzio, F., Ribera d’Alcalà, M., Pulido-Villena, E., 2020.  
644 Profiling float observation of thermohaline staircases in the western Mediterranean Sea and  
645 impact on nutrient fluxes. *Biogeosciences* 17, 3343–3366. [https://doi.org/10.5194/bg-17-3343-](https://doi.org/10.5194/bg-17-3343-2020)  
646 [2020](https://doi.org/10.5194/bg-17-3343-2020)
- 647 Thurnherr, A.M., 2022. How to Process LADCP Data For Vertical Velocity ( $w$ ) and Derive  
648 Parameterized Estimates for Turbulent Kinetic Energy Dissipation ( $\epsilon$ ) using LADCP w  
649 Software V2.2.
- 650 Thurnherr, A.M., 2021. How To Process LADCP Data With the LDEO Software (Version  
651 IX.14).
- 652 Verso, L., Reeuwijk, M.V., Liberzon, A., 2019. Transient stratification force on particles  
653 crossing a density interface. *International Journal of Multiphase Flow* 121, 103109.  
654 <https://doi.org/10.1016/j.ijmultiphaseflow.2019.103109>
- 655 Wakeham, S.G., Lee, C., 1993. Production, Transport, and Alteration of Particulate Organic  
656 Matter in the Marine Water Column, in: Engel, M.H., Macko, S.A. (Eds.), *Organic*  
657 *Geochemistry, Topics in Geobiology*. Springer US, Boston, MA, pp. 145–169.  
658 [https://doi.org/10.1007/978-1-4615-2890-6\\_6](https://doi.org/10.1007/978-1-4615-2890-6_6)



659 WET Labs, Inc., 2011. Transmissometer C-Star User's Guide.

660 Zodiatis, G., Gasparini, G.P., 1996. Thermohaline staircase formations in the Tyrrhenian Sea.  
661 Deep Sea Research Part I: Oceanographic Research Papers 43, 655–678.  
662 [https://doi.org/10.1016/0967-0637\(96\)00032-5](https://doi.org/10.1016/0967-0637(96)00032-5)

663

664

#### 665 **Data Availability Statement**

666 The CTD and ADCP data used in this study are available at  
667 <https://doi.org/10.17600/18001342>. The UVP data are available at <https://ecopart.obs-vlfr.fr>.

668

#### 669 **Author Contributions**

670 Conceptualization and Methodology, XDDM, PB and MPP; Writing – Original Draft  
671 Preparation, XDDM and PB; Writing – Review & Editing, All.

672

#### 673 **Acknowledgements**

674 This study benefited from the data obtained during the PERLE-3 cruise with the R/V  
675 Pourquoi-Pas? and was supported by the MISTRALS-MERMEX project.

676

#### 677 **Competing interests**

678 The authors declare that they have no conflict of interest.